Electrodeposition and selenization of brass/tin/germanium multilayers for $Cu_2Zn(Sn_{1-x}Ge_x)Se_4$ thin film photovoltaic devices

Kwinten Clauwaert[a,b], Maaike Goossens[a], Jessica De Wild[c], Diego Colombara[c], Phillip J. Dale[c], Koen Binnemans[d], Edward Matthijs[a,*], Jan Fransaer[b,*]

[a] KU Leuven, Faculty of Engineering Technology, Cluster Sustainable Chemical Process Technology, Technology Campus Gent, Gebroeders Desmetstraat 1, B-9000 Gent, Belgium
[b] KU Leuven, Department of Materials Engineering, Kasteelpark Arenberg 44, P.O. Box 2450, B-3001 Leuven, Belgium
[c] Physics and Materials Science Research Unit, University of Luxembourg, rue du Brill 41, L-4422 Belvaux, Luxembourg
[d] KU Leuven, Department of Chemistry, Celestijnenlaan 200F, P.O. Box 2404, B-3001 Leuven, Belgium

ABSTRACT

Dense, closed, homogeneous brass/tin/germanium multilayers have been prepared by electrochemical methods. The stacks were electrodeposited on molybdenum-sputtered soda-lime glass. Brass was deposited first from an aqueous pyrophosphate electrolyte. Then, tin was deposited from a tin(II) pyrophosphate electrolyte. Germanium was deposited as the top film from 5 vol% $GeCl_4$ in propylene glycol. The composition of the brass/tin/germanium stack could easily be controlled by adjustment of the charge of the deposition of each coating and with special attention to exchange reactions. The variation in film thickness was minimized by using a rotating disk electrode (RDE) sample holder with a current thief. Soft-annealing under a nitrogen atmosphere and selenization with elemental selenium resulted in dense, closed copper-poor and zinc-rich CZTGSe absorber material. P-type conductivity was confirmed by photoelectrochemistry and a first photovoltaic device showed a power conversion efficiency of 0.6% and a band gap near 1.2 eV (with Ge/(Sn + Ge) = 0.38).

© 2016 Elsevier Ltd. All rights reserved.

1. Introduction

Thin film photovoltaics based on Cu(In,Ga)(S,Se)$_2$ (CIGS) and CdTe have recently attained power conversion efficiencies of 22.3% [1] and 21.0% [2], respectively, and are deployed on an industrial scale. However, both types of photovoltaic devices face long-term sustainability issues because of the health risks of cadmium and the scarcity of indium, gallium and tellurium [3,4]. In recent years, $Cu_2ZnSn(S,Se)_4$ (CZT(S,Se)) thin films are investigated as an alternative for CIGS because of their similar optoelectronic properties and more abundant and environmentally benign elements. The crystal structure of this material is obtained by replacing half of the indium and gallium atoms in CIGS by zinc atoms and the other half by tin atoms, which are both more earth-abundant materials [5,6]. The CZT(S,Se) compound is a *p*-type semiconductor with a large absorption coefficient of over 10^4 cm^{-1} and a band gap between 0.95 eV and 1.5 eV depending on the

sulfur-to-selenium ratio [7]. The record efficiency for a CZTSSe device of 12.6% was obtained by Wang et al. by a hydrazine-based spin-coating process [8]. However, sulfur and selenium are volatile species, so controlling the exact compositions, thus exact band gap, is difficult. Alternatively, the band gap of CZT(S,Se) can be tuned by (partial) replacement of tin by germanium ($Cu_2Zn(Sn_{1-x}Ge_x)(S,Se)_4$ or CZTG(S,Se)). With a concentration in the Earth's crust of approximately 1.5 ppm, germanium is slightly more abundant than tin [9]. Because it is only mined as a by-product of mainly zinc ores and coal, its price is significantly higher than that of tin [10,11]. It must be taken into account that only small amounts of germanium (and tin) are required for the production of CZTGSe. Furthermore, research on the recovery of germanium from (electronic) devices is performed in order to increase the elements availability and to control and decrease its price [12]. Tin and germanium can both be electrodeposited and are significantly less volatile than sulfur and selenium. Band gap tuning of kesterite type absorber layers is therefore preferably performed by altering the tin-to-germanium ratio because this ratio can be more easily controlled, enabling the production of semiconductors with a specific band gap. The band gap for a sulfur-free device is tunable from 0.95 eV ($Cu_2ZnSnSe_4$) [13] to 1.6 eV ($Cu_2ZnGeSe_4$) [14]. A maximum band gap of 2.2 eV is

---

obtained in a selenium-free and tin-free Cu_2ZnGeS_4 device [15]. The presence of multivalent tin in CZT(S,Se) is associated with deep level traps in the absorber material. Germanium can also occur in the +II and +IV oxidation state, but the +II form is unlikely. Therefore, partial replacement of tin by germanium can theoretically lead to improved optoelectronic properties by the reduction of deep level traps [16]. Furthermore, alloying with germanium appears to enhance the performance of CZTS photovoltaic devices by increasing minority charge carrier lifetimes and reducing voltage-dependent charge carrier collection. Hages et al. produced CZTG(S,Se) devices without germanium and with partial replacement of the tin by germanium. Replacement of 30% of the tin by germanium resulted in a 1% absolute improvement of the light to electricity conversion efficiency and a 50 mV increase of the open circuit voltage [17]. CZTG(S,Se) thin films are commonly prepared by nanocrystal ink doctor-blading [17–19], evaporation [14,20], sputtering [21] and spin-coating [22]. The record CZTGSSe device was prepared by a nanocrystal ink-annealing method and had a power conversion efficiency of 9.4% with Ge/(Sn + Ge) = 0.3 [17]. This new record stimulates research on production techniques that are more environmentally benign and offers perspectives for application on a large scale.

In this view, electrodeposition is a promising technique because it is a low-cost method that allows fast and continuous production on large substrates with good control over the composition and morphology [23]. Three approaches are commonly used to deposit the precursors for CZT(S,Se) thin films and are interesting for the development of CZTG(S,Se) thin films as well: successive deposition of elemental or binary alloy coatings, co-electrodeposition of the metals and co-electrodeposition of the metals and sulfur/selenium. After deposition of these films, an annealing step is required to sulfurize/selenize the precursors and/or improve the optoelectronic properties of the films.

Although simultaneous electrodeposition of all metals and chalcogen co-electrodeposition require only a minimum of equipment and process steps, further deployment of these techniques is hindered by the difficult process control. Addition of germanium as a fourth or fifth element to be incorporated, will only further impede the process control. Electrodeposition of stacked elemental and/or binary alloy coatings overcomes these issues. This method implies several deposition and rinsing steps, thus requiring a higher equipment cost. However, this disadvantage does not exceed the benefits of the technique. The most important advantage is the high degree of control of the final composition of the stack by changing the thickness of each coating [24]. Here, the variation in film thickness, responsible for in-depth inhomogeneity, was minimized by artificially enlarging the substrate with a current thief that surrounded the molybdenum substrate. Each deposition step can be optimized separately, enabling the deposition of uniform, dense films on large areas from stable electrolytes and short deposition times [23]. For the electrodeposition of brass and tin from aqueous electrolytes, several well-described electrolytes that are used on an industrial scale, are available [25]. On the contrary, the electrodeposition of germanium from aqueous electrolytes is difficult due to the low hydrogen overpotential on germanium [26]. Electrolytes based on organic solvents (e.g. propylene glycol) are typically used [27] and more recently, ionic liquids are investigated for the electrodeposition of germanium with the aim to completely impede hydrogen formation [28,29].

In this paper, dense, closed, homogeneous brass/tin/germanium multilayers were prepared by electrochemical methods. Brass and tin were deposited from aqueous electrolytes, while germanium was deposited from a propylene glycol electrolyte. The deposition conditions of each coating were tuned with special focus on the process control. The brass/tin/germanium stacks were

soft-annealed under a nitrogen atmosphere and selenized with elemental selenium in order to produce CZTGSe thin films for photovoltaic devices. With Cu/(Zn + Sn + Ge), Zn/(Sn + Ge) and Ge/(Sn + Ge) atomic ratios after selenization of 0.85, 1.10 and 0.38, respectively, the targeted ratios for the kesterite structure were reached by this novel approach.

2. Experimental

2.1. Electrolytes

The electrodeposition of brass was performed from an aqueous electrolyte containing $0.012 \text{ mol dm}^{-3}$ copper(II) pyrophosphate ($Cu_2P_2O_7 \cdot 3H_2O$, Sigma-Aldrich), $0.210 \text{ mol dm}^{-3}$ zinc(II) sulfate ($ZnSO_4 \cdot 7H_2O$, Acros Organics > 99.5%) and $0.550 \text{ mol dm}^{-3}$ potassium pyrophosphate ($K_4P_2O_7$, Sigma-Aldrich 97%). The pH was adjusted to 10 with ortho-phosphoric acid (H_3PO_4, Carl Roth $\geq$ 85% pro analysis). After dissolution and adjustment of the pH, the electrolyte was deaerated with nitrogen.

Tin was deposited from an aqueous tin(II) electrolyte containing 0.01 mol dm^{-3} tin(II) pyrophosphate ($Sn_2P_2O_7$, Sigma-Aldrich 98%) and 0.20 mol dm^{-3} potassium pyrophosphate. The pH was adjusted to 10 with ortho-phosphoric acid. Afterwards, the electrolyte was deaerated with nitrogen.

Germanium was deposited from 5 vol% germanium(IV) chloride ($GeCl_4$, Umicore, Olen (Belgium) 99.99 %) in propylene glycol ($C_3H_8O_2$, Acros Organics 99%). Germanium(IV) chloride was used as received. Propylene glycol was dried in a vacuum of 0.6 mbar at room temperature for 24 h. The electrolyte was prepared and handled in an argon-filled glove box (oxygen and water content below 1 ppm).

2.2. Electrodeposition

Prior to the electrodeposition of brass, the molybdenum substrate was cleaned by immersion in ethanol (Chem-Lab) for 5 min at 22 °C, rinsing with water, immersion in a 12.5 wt% ammonia solution (Merck) for 5 min at 22 °C and rinsing with water again. After each electrodeposition procedure, the working electrode was rinsed with water and ethanol and dried with air ($\pm$ 40 °C). Before the deposition of tin, it was immersed in ethanol for 5 min at 22 °C and rinsed with water. Before the deposition of germanium, the sample was immersed in ethanol for 5 min at 22 °C without subsequent rinsing with water.

Chronoamperometric electrodepositions of brass and tin were performed in a 1000 mL three-electrode cell. The electrodeposition conditions are summarized in Table 1. An inert counter electrode consisting of a titanium grid coated with RuO_2/IrO_2 (dimensionally stable anode, DSA) covered the complete bottom of the electrolysis cell. A Ag|AgCl (3 M KCl) electrode (+0.210 V vs. SHE; Microelectrodes, Inc. MI-402) was used as the reference and was placed in the immediate vicinity of the working electrode. In this manuscript, all potentials are expressed versus SHE. Molybdenum-sputtered SLG plates (Guardian EcoGuard® Mo) of $20 \times 20 \text{ mm}^2$ were used as working electrode. The working

Table 1
Electrodeposition parameters for brass, tin and germanium coatings.

Coating	Cu-Zn	Sn(II)	Ge[*]
T/°C	22	22	22
E/V vs. SHE	−1.29	−1.19	–
j/A dm^{-2}	–	–	−10
ω/rpm	175	250	Mild stirring

[*] The germanium electrolyte was prepared and handled in a glove box (oxygen and water content below 1 ppm).

electrode was mounted in a RDE system (Fig. 1) with a CTV 101 speed control unit (Radiochemie, Analysis). The variation in film thickness was minimized by artificially enlarging the surface of the substrate using a stainless steel current thief (Ø = 40 mm) that surrounded the molybdenum working electrode. All electrodes were connected to a Bio-Logic SP-200 potentiostat equipped with EC-Lab® software (V10.23).

Germanium was chronopotentiometrically deposited on top of the brass/tin stack in a 100 mL two-electrode cell at 22 °C. The deposition parameters are summarized in Table 1. The electrodeposition conditions were based on the work of Saitou et al. [27]. In their work, the electrolyte was not dried before use and was not agitated during deposition. However, in our experiments, better adhering films were deposited when the electrolyte was dried as described in section 2.1 "Chemicals" and when it was mildly agitated with a magnetic stir bar during deposition. The working electrode was mounted vertically in the cell. A graphite counter electrode with a significantly larger area than the working electrode was used.

2.3. Cyclic voltammetry and linear sweep voltammetry

Cyclic voltammetry of the brass electrolyte was performed at 22 °C in 0.012 mol dm^{-3} Cu$_2$P$_2$O$_7$ and 0.550 mol dm^{-3} K$_4$P$_2$O$_7$, 0.210 mol dm^{-3} ZnSO$_4$ and 0.550 mol dm^{-3} K$_4$P$_2$O$_7$ and 0.012 mol dm^{-3} Cu$_2$P$_2$O$_7$, 0.210 mol dm^{-3} ZnSO$_4$ and 0.550 mol dm^{-3} K$_4$P$_2$O$_7$. The pH of all electrolytes was adjusted to pH = 10. Cyclic voltammetry of the tin electrolyte was performed in 0.01 mol dm^{-3} Sn$_2$P$_2$O$_7$ and 0.20 mol dm^{-3} K$_4$P$_2$O$_7$ (22 °C, pH = 10). House-made disk electrodes of molybdenum (Ø = 3.0 mm) and copper (Ø = 2.0 mm) embedded in a PVDF tip were used for cyclic voltammetry in the brass and tin electrolytes, respectively. The electrodes were consecutively polished with 15 μm and 3 μm diamond suspensions and a 0.05 μm alumina suspension on a polishi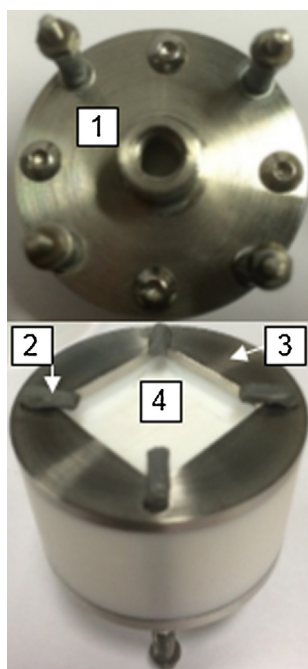ng cloth (BASi). Next, the electrodes were rinsed with water in an ultrasonic bath in order to remove residual particles. Finally, the pretreatment described in section 2.2 "Electrodeposition" was performed. A DSA counter electrode and a Ag|AgCl (3 M KCl) reference electrode were used. All cyclic voltammograms were recorded at a scan speed of 15 mV s^{-1}.

Linear sweep voltammetry (LSV) was performed in order to study the electrochemical behavior of deposited brass films in 0.2 mol dm^{-3} K$_4$P$_2$O$_7$ at 22 °C (pH = 10). Prior to LSV, brass was plated on molybdenum-sputtered SLG plates from 0.012 mol dm^{-3} Cu$_2$P$_2$O$_7$, 0.210 mol dm^{-3} ZnSO$_4$ and 0.550 mol dm^{-3} K$_4$P$_2$O$_7$ (pH = 10) at 22 °C, a deposition potential of −1.29 V, a rotation speed of 175 rpm and a charge density of 3.5 10^4 C m^{-2}. The brass-plated substrate was used as working electrode for LSV. A DSA counter electrode and a Ag|AgCl (3 M KCl) reference electrode completed the three-electrode cell. After immersion of the working electrode, the potential was swept from −1.2 V to 0.5 V at a scan speed of 50 mV s^{-1}.

2.4. Soft-annealing, selenization and photovoltaic device fabrication

The brass/tin/germanium stacks were soft-annealed in a tube furnace under a nitrogen atmosphere. After placing the samples in the oven, the temperature was increased from 22 °C to 350 °C at 1 °C s^{-1} and held at 350 °C for 60 min. After cooling to ambient temperature under a nitrogen atmosphere, they were transferred to a graphite box together with elemental selenium pellets (99.999 + %). The box was placed in a nitrogen-filled tube furnace, heated from 22 °C to 500 °C at 1 °C s^{-1}, held constant for 40 min and cooled to ambient temperature under a nitrogen atmosphere. After optimization of the consecutive etching with KCN and HCl (cfr. 2.5 "Characterization of the films"), the samples were processed into complete photovoltaic devices with standard CdS/i-ZnO/Al:ZnO buffer layers and Ni/Al grid. The deposition of these layers was performed as described by Aida et al. [30].

2.5. Characterization of the films

The global compositions were determined by analysis of the copper, zinc, tin and germanium content by inductively coupled plasma optical emission spectroscopy (ICP-OES, Varian 720 ES) after dissolving the samples in *aqua regia*. Local determinations and analysis of the morphology were done with energy-dispersive X-ray spectroscopy (EDX, EDAX Genesis 4000) combined with scanning electron microscopy (SEM, Philips XL 30 FEG). X-ray diffraction (XRD, Seifert 3003) was used to characterize the crystal structure of as-deposited, soft-annealed and selenized films.

Photoelectrochemical characterization (PEC) of selenized samples were performed with a set-up described in [31] using a 0.2 mol dm^{-3} europium nitrate (Eu(NO$_3$)$_3$, Alfa Aesar 99.9%) aqueous electrolyte as the electron scavenging species. The film was subject to several consecutive etching treatments with 5 wt% potassium cyanide (KCN, Sigma-Aldrich ≥ 98%) and 5 wt% hydrochloric acid (HCl, Sigma-Aldrich 36.5–38.0 wt% solution in water) solutions. It must be noted that potassium cyanide and hydrochloric acid should never be used simultaneously in the same fume hood as this will lead to formation of highly poisonous hydrogen cyanide gas. Chronoamperometric measurements were performed under the flashed light of a 530 nm LED at an illumination intensity equivalent to 2% of AM1.5, with the photoelectrodes held at −0.59 V vs SHE.

Finished photovoltaic devices were characterized by current–voltage measurements using a four point probe configuration with an AM1.5 intensity-equivalent illumination (1000 W m^{-2}, 25 °C) calibrated with a 13.0 ± 0.2% efficient monocrystalline silicon solar cell (certified by VLSI Standards Inc.). External quantum efficiency (EQE) spectra were recorded by illumination of the photovoltaic

Fig. 1. Sample holder for the electrodeposition of brass on molybdenum-sputtered SLG (20 × 20 mm²) and tin on brass. 1: connection to rotation axis; 2: clamp for electrical contact; 3: stainless steel current thief; 4: place for mounting the substrate.

devices with monochromatic light of variable wavelength optically chopped at 130 Hz. The photocurrent was measured with a digital lock-in amplifier (Stanford Research SR 850). The system was calibrated with standardized silicon and indium-gallium-arsenide photodiodes.

3. Results and discussion

3.1. Brass coating

In previous work, we investigated the electrochemical behavior of molybdenum in a 0.5 mol dm^{-3} potassium pyrophosphate solution at pH = 10 [32]. Under these circumstances, molybdenum has the tendency to form a surface film of MoO$_2$ [33], which impedes good adhesion of the deposited metals. Therefore, a pretreatment of the substrate was developed. First, immersion in an ammonia solution removed MoO$_2$ from the surface [34]. After rinsing the substrate with water, it was immersed in the plating bath and a potential of 0.11 V was applied for 15 s, resulting in an anodic current. Adherent brass films could only deposited on the molybdenum substrate after performing this pretreatment procedure. Without the pretreatment, parts of the brass films peeled off from the molybdenum substrate.

Brass was deposited from a pyrophosphate electrolyte at pH = 10. This pH was chosen empirically because of the difficulty to deposit dense, closed films with the desired composition at lower pH values. At higher pH values, insoluble species destabilize the electrolyte by the formation of precipitates. At pH = 10, [Cu(P$_2$O$_7$)$_2$]$^{6-}$ and [Zn(P$_2$O$_7$)$_2$]$^{6-}$ are the dominant metal pyrophosphate complexes [32]. These highly negative complexes do not exist as such, but associate with potassium ions as K$_x$ML$_n$$^{(4x-2-x)-}$ complexes [35]. The standard reduction potentials of the dominant complexes were calculated by application of Hess's law and the relation between the Gibbs free energy, complex formation equilibrium constants ($\log(K_{[Cu(P_2O_7)_2]^{6-}})$ = 12.45 and $\log(K_{[Zn(P_2O_7)_2]^{6-}})$ = 11.00 [36]) and standard reduction potential of the uncomplexed metal. Next, the reduction potentials of [Cu(P$_2$O$_7$)$_2$]$^{6-}$ and [Zn(P$_2$O$_7$)$_2$]$^{6-}$ under the circumstances presented in this work, were calculated by using the Nernst equation and were found to be −0.02 V and −1.05 V, respectively. Because of the large difference between the reduction potentials, electrodeposition of high-quality brass was not expected. However, the reduction rate of copper(II) is kinetically hindered due to adsorption of pyrophosphate on the surface of the electrode [37–39]. Johannsen et al. confirmed this phenomenon during electrochemical quartz microbalance experiments (EQCM) by observing a decrease in the crystal's frequency around −0.65 V vs. SCE without measuring a current [39]. They attributed this observation to the adsorption of non-electroactive pyrophosphate species. Because pyrophosphate ions are negatively charged, the degree of adsorption decreases with decreasing potential, enabling appreciable copper deposition currents at potentials that are rather negative compared to the thermodynamic potential. Cyclic voltammetry in a copper(II) pyrophosphate electrolyte on a molybdenum disk working electrode confirmed the slow kinetics (Fig. 2(Cu)). At potentials more negative than −0.29 V, a broad peak was recorded due to the slow reduction of copper(II). The copper deposition rate increased at −0.78 V, hence appreciable currents were only achievable at significantly more negative potentials than the calculated −0.02 V. Because of the kinetic hindrance, the difference between the reduction potentials of copper(II) and zinc(II) in the pyrophosphate electrolyte decreased, making this electrolyte a suitable brass plating bath. After reversing the scan direction, a nucleation loop was recorded followed by the cross-over point at −0.24 V. Because the stripping of copper and the
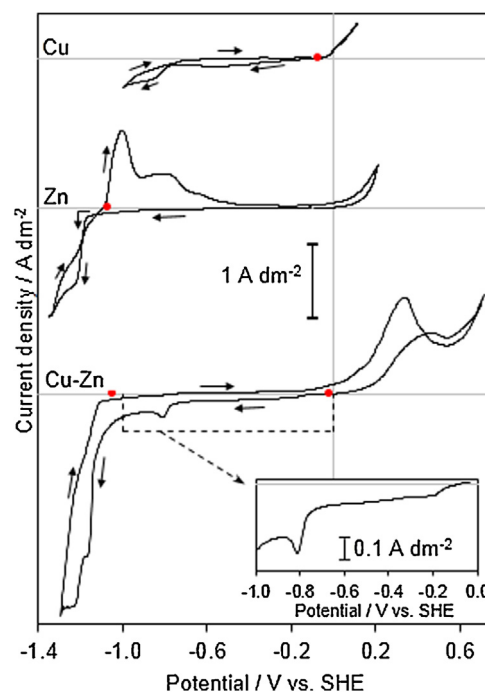

Fig. 2. Cyclic voltammograms (scan speed 15 mV s^{-1}) of 0.012 mol dm^{-3} Cu$_2$P$_2$O$_7$ + 0.550 mol dm^{-3} K$_4$P$_2$O$_7$; 0.210 mol dm^{-3} ZnSO$_4$ + 0.550 mol dm^{-3} K$_4$P$_2$O$_7$ and 0.012 mol dm^{-3} Cu$_2$P$_2$O$_7$ + 0.210 mol dm^{-3} ZnSO$_4$ + 0.550 mol dm^{-3} K$_4$P$_2$O$_7$ (pH = 10) at 22 °C. Molybdenum disk working electrode (Ø = 3.0 mm), DSA counter electrode and Ag|AgCl (3 M KCl) reference electrode. ● Calculated reduction potentials of the dominant copper(II) and zinc(II) pyrophosphate complexes. The zero current lines are represented by gray horizontal lines.

oxidation of molybdenum overlapped, no copper stripping peak was recorded.

The cyclic voltammogram of a zinc(II) pyrophosphate electrolyte is shown in Fig. 2(Zn). Zinc was deposited at potentials more negative than −1.15 V and was accompanied by hydrogen gas formation. A nucleation loop was recorded after reversing the scan direction. The cross-over point was reached at −1.09 V, which corresponds well to the calculated −1.06 V. The stripping of the zinc coating was recorded as two oxidation peaks. After the negative scan, the scan direction was reversed at potentials at which significant hydrogen gas formation occurred. The reduction of water to hydrogen gas is accompanied by the production of hydroxide ions. Because the electrolyte was not agitated during cyclic voltammetry, the hydroxide ions significantly increased the pH near the electrode surface and could result in the precipitation of Zn(OH)$_2$. During the reversed scan, the oxidation could be disrupted by the presence of this precipitated Zn(OH)$_2$ layer, which could lead to two oxidation peaks. It is also possible that, due to hydrogen gas formation, the morphology of the zinc deposit differed significantly from the zinc deposited at potentials at which significantly less hydrogen gas formation occurred, resulting in different dissolution kinetics. A similar behavior was observed by Sylla et al. for the electrodeposition of Zn-Mn alloys [40].

Fig. 2(Cu-Zn) shows the cyclic voltammogram in the binary electrolyte. During the negative scan, three reduction peaks were recorded. The first was a broad peak starting at −0.16 V and was related to the slow reduction of copper(II) in the potential region where pyrophosphate adsorption occurs. At −0.77 V, the copper(II) reduction rate increased and a second reduction peak was observed. The reductive current increased again at −1.05 V due to the simultaneous reduction of zinc(II), followed by hydrogen gas formation at potentials more negative than −1.29 V. After

reversing the scan direction, the cross-over was reached at −0.75 V. This value is situated between the calculated reduction potentials of copper(II) and zinc(II) (−0.02 V and −1.05 V, respectively) which suggested the deposition of a copper-zinc alloy during the negative scan. The current did not further increase until −0.11 V, followed by stripping of the alloy, of the underlying copper coating and formation of oxygen gas. After removing the disk electrode from the electrolyte, a residual deposit was observed on the electrode surface, hence a fraction did not dissolve during the positive scan.

Scragg et al. observed significant variations in film thickness over the surface of electrodeposited copper/tin/zinc stacks, leading to inhomogeneities on the micron to millimeter range after sulfurization [41]. Kurihara et al. reduced the variation in film thickness by performing electrodeposition experiments under hydrodynamic control with a RDE [42]. In our work, a stainless steel current thief, surrounding the molybdenum electrode, was added to the RDE in order to minimize variation in film thickness. Without the current thief, the thickness of the brass films varied from approximately 800 nm near the edges to 450 nm in the center. Using the current thief, a uniform brass film with a thickness of 640 ± 24 nm was obtained. Mirror-bright, yellowish coatings with 60 at% copper were deposited (Fig. 3a). SEM analysis showed that fine-grained, dense, closed, adherent coatings were obtained (Fig. 3b,c). Furthermore, electrodeposition of brass coatings at different charge densities showed that the thickness increased linearly as a function of the charge density ($R^2 = 0.98$) and that the composition of the coatings did not significantly vary with increasing thickness (copper content = 57.5 ± 0.7 at%) (Fig. 4). The high degree of control over the composition and thickness of the coating, the microscopic uniformity and good adhesion to the molybdenum substrate facilitated the subsequent deposition of other coatings.
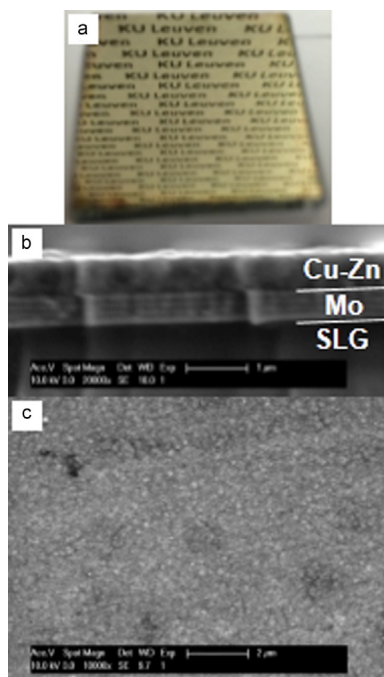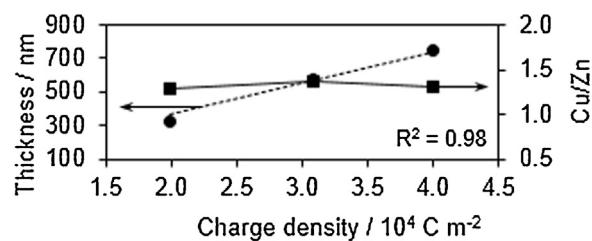

Fig. 4. Thickness (●) and composition of the brass coating (■) as a function of deposition charge density. Deposition from 0.012 mol dm^{-3} Cu$_2$P$_2$O$_7$, 0.210 mol dm^{-3} ZnSO$_4$ and 0.550 mol dm^{-3} K$_4$P$_2$O$_7$, E$_{dep.}$ = −1.29 V vs. SHE, ω = 175 rpm, T = 22 °C.

3.2. Tin coating

Tin was deposited on top of the brass coatings from a tin(II) pyrophosphate electrolyte. The reduction potential of the dominant complex [Sn(P$_2$O$_7$)$_3$]$^{10-}$ was calculated by the method in section 3.1 "Brass coating" ($\log(K_{[Sn(P_2O_7)_3]^{10-}})$ = 18.40 [43]) and was found to be −0.66 V.

The cyclic voltammogram of the tin plating bath is shown in Fig. 5. Cyclic voltammetry in the tin(II) pyrophosphate electrolyte showed that tin deposition occurred at potentials more negative than −1.00 V. After reversing the scan direction, the cross-over was reached at −0.66 V, which corresponded to the calculated potential. Next, the oxidation peak of the tin coating was recorded. Because of incomplete stripping (Q$_{anodic}$/Q$_{cathodic}$ = 37%), no increase of the anodic current due to the oxidation of the electrode material was recorded. According to the Pourbaix diagram, tin has the tendency to form a passive film of SnO$_2$ at its surface between pH 1.0 and 12.5 [44]. This film protected the substrate material from oxidizing. After removal from the electrolyte, a silvery gray coating was observed on the electrode, which demonstrated the incomplete dissolution of the tin coating.

A copper/tin/zinc stacking order is typically used for electrochemical preparation of CZTS solar cells by the SEL approach. Other stacking orders often lead to metal exchange reactions and partial stripping of the coating during consecutive plating steps because of the relative positions of the standard reduction potentials of copper, tin and zinc [24,45]. In order to avoid metal exchange reactions, electrodeposition procedures should be developed that enable the deposition of adherent, uniform coatings at rather negative potentials. Ideally, the electrolytes leave the underlying material unharmed. Therefore, the suitability of the tin(II) pyrophosphate was studied by performing anodic LSV on the brass deposits in tin(II)-free pyrophosphate electrolytes (Fig. 6).
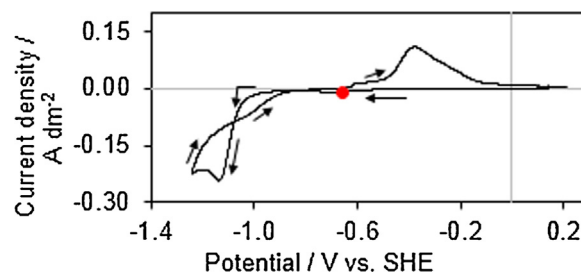

Fig. 3. Image (a), cross-section (b) and top-view SEM image (c) of a brass coating on molybdenum-sputtered SLG (20 × 20 mm^2) obtained from 12 mmol dm^{-3} Cu$_2$P$_2$O$_7$, 210 mmol dm^{-3} ZnSO$_4$ and 550 mmol dm^{-3} K$_4$P$_2$O$_7$ (pH = 10) at 22 °C. E$_{dep.}$ = −1.29 V vs. SHE, ω = 175 rpm, Q = 2.5 10^4 C m^{-2}.

Fig. 5. Cyclic voltammogram (scan speed 15 mV s^{-1}) of 0.01 mol dm^{-3} Sn$_2$P$_2$O$_7$ + 0.20 mol dm^{-3} K$_4$P$_2$O$_7$ (pH = 10) at 22 °C. Copper disk working electrode (Ø = 2.0 mm), DSA counter electrode and Ag|AgCl (3 M KCl) reference electrode. ● Calculated reduction potential of the dominant tin(II) pyrophosphate complexes.
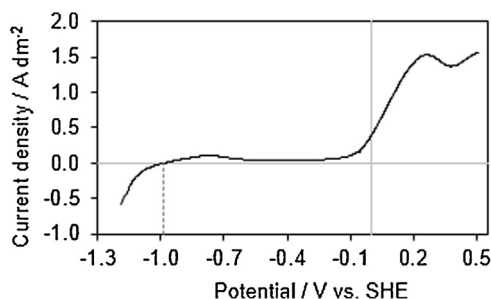
Fig. 6. Anodic linear sweep voltammogram (scan speed $50 \, mV \, s^{-1}$) of a brass coating on molybdenum-sputtered SLG in $0.2 \, mol \, dm^{-3} \, K_4P_2O_7$ at $22 \, °C$ (pH = 10). Scan from $-1.2 \, V$ to $0.5 \, V$.

Table 2

Composition of brass before the electrodeposition of tin (Cu-Zn) and composition of brass/tin stacks after electrodeposition of tin (Sn(II)) from $0.01 \, M \, Sn_2P_2O_7 + 0.20 \, M \, K_4P_2O_7$, pH = 10, T = 22 °C on brass-coated molybdenum-sputtered SLG (ICP-OES).

Electrolyte	Cu-Zn	Sn(II)[*]
Cu/at%	54	49 (54)
Zn/at%	46	41 (46)
Sn/at%	–	10 (–)

[*] The values between brackets are the copper and zinc fractions without taking the tin content into account.

The cross-over was reached at $-0.99 \, V$ and fast dissolution of the brass coating occurred at potentials more positive than $-0.14 \, V$. Because the reduction of tin(II) is thermodynamically expected at $-0.66 \, V$, compositional changes of the brass coatings by exchange reactions after immersion in the tin electrolyte were expected. As-deposited brass coatings were immersed in a tin(II) pyrophosphate electrolyte for 1 to 20 min and the compositional changes were analyzed with ICP-OES (Fig. 7). The amount of copper in the coating did not change by immersion in the electrolyte. The increasing tin content and decreasing zinc content in the coating demonstrated the exchange reaction between zinc and tin. $Sn^{2+} + Zn \rightarrow Sn + Zn^{2+}$ was the expected exchange reaction, hence a Δzinc-to-Δtin ratio of 1 should be obtained (with Δelement = the mass of the element in the coating after immersion subtracted by the mass of the element in the as-deposited coating). Analysis of the composition showed that this ratio varied between 1.46 and 4.34, hence the coating was simultaneously affected by another reaction. Therefore, as-deposited brass coatings were immersed in a tin(II)-free pyrophosphate electrolyte for 1 to 10 minutes. Between pH values of 8.5 and 10.5, zinc has the tendency to cover itself with a film of $Zn(OH)_2$, which is only slightly soluble [46]. However, the formation of this film is inhibited by alloying zinc with another metal, allowing (slow) dissolution of zinc with the formation of hydrogen gas. Because of the high solubility of the $[Zn(P_2O_7)_2]^{6-}$ complex, the dissolution of zinc is further promoted. This resulted in significant losses of zinc by immersion of brass coatings in a pyrophosphate solution at pH = 10 (Fig. 7). At short immersion times in tin(II) pyrophosphate electrolytes, the loss of zinc was predominantly caused by the dissolution reaction. Longer immersion times, thus more profound exchange reaction between solid zinc and Sn^{2+} ions in solution, enabled a higher degree of coverage of the electrode surface by solid tin which inhibited the
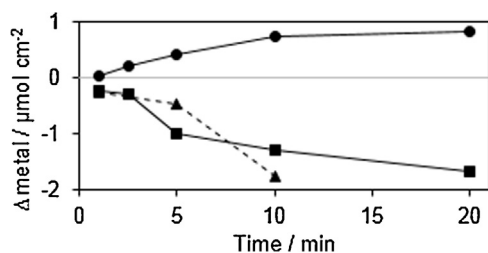
chemical dissolution of zinc. This is demonstrated by the significantly smaller loss of zinc after 10 min immersion in a tin (II) pyrophosphate electrolyte compared to the loss of zinc after 10 min immersion in a tin(II)-free pyrophosphate electrolyte. The exchange reaction was completely inhibited after formation of a tin coating of approximately $0.8 \, \mu mol \, cm^{-2}$, i.e. approximately 130 nm, on the electrode surface.

In order to avoid exchange reactions and chemical dissolution, the substrate was cathodically protected by using hot entry, i.e. the deposition potential was applied before immersion of the substrate in the electrolyte. Analysis with ICP-OES of the coatings deposited by this procedure showed that no zinc and/or copper losses occurred (Table 2).

The electrodeposited tin coatings showed good adhesion to the brass coating and had a lustrous gray color (Fig. 8a). A deposition potential of $-1.19 \, V$ and a rotation speed of 250 rpm resulted in dense, closed coatings with good adhesion to the brass coating (Fig. 8b,c). The tin coating thickness increased linearly as a function
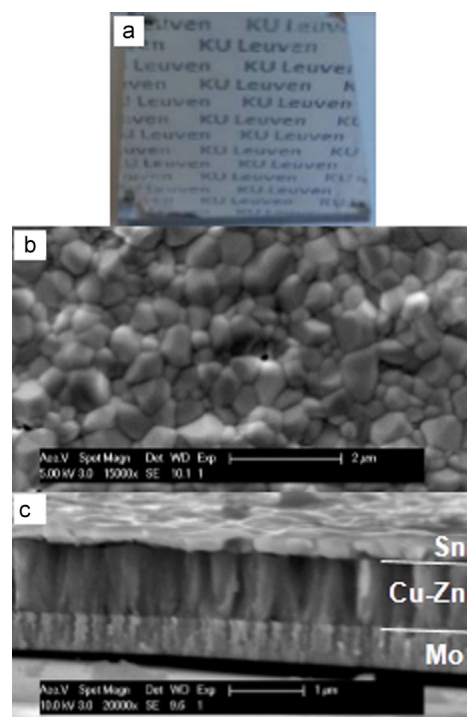

Fig. 7. Tin increase (●) and zinc decrease (■) of electrodeposited brass as a function of time after immersion in $0.01 \, M \, Sn_2P_2O_7 + 0.20 \, M \, K_4P_2O_7$, pH = 10, T = 22 °C (solid line) and zinc decrease (▲) after immersion in $0.20 \, M \, K_4P_2O_7$, pH = 10, T = 22 °C (dashed line). Δmetal = $n_{after \, immersion} - n_{before \, immersion}$ with n = the amount of the respective metal in $\mu mol \, cm^{-2}$. Analysis with ICP-OES.

Fig. 8. Image (a), top-view (b) and cross-section (c) SEM images of tin deposited on a brass coating on molybdenum-sputtered SLG ($20 \times 20 \, mm^2$). Deposition from $0.01 \, mol \, dm^{-3} \, Sn_2P_2O_7$ and $0.20 \, mol \, dm^{-3} \, K_4P_2O_7$ (pH = 10), $E_{dep.} = -1.19 \, V$ vs. SHE, $\omega = 250 \, rpm$, T = 22 °C.
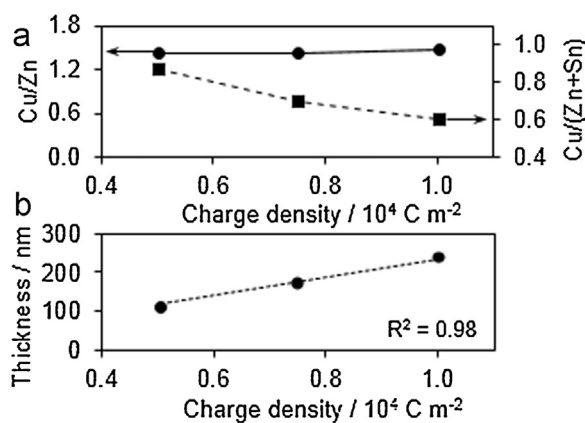
Fig. 9. Cu/Zn ($\bullet$) and $Cu/(Zn + Sn)$ ($\blacksquare$) of the coating after electrodeposition of tin (a) and thickness of the tin coating (b) as a function of deposition charge density. Deposition of tin from $0.01\,mol\,dm^{-3}\,Sn_2P_2O_7$ and $0.20\,mol\,dm^{-3}\,K_4P_2O_7$ (pH = 10), $E_{dep.} = -1.19\,V$ vs. SHE, $\omega = 250\,rpm$, $T = 22\,°C$.

of the deposition charge density ($R^2 = 0.98$), hence the composition of the brass/tin stack could easily be controlled by controlling the deposition charge density (Fig. 9).

3.3. Germanium coating

The electrodeposition of germanium from 5 vol% $GeCl_4$ in propylene glycol was performed on molybdenum, on brass-coated molybdenum and on brass/tin-coated molybdenum. Due to excessive hydrogen gas formation during the electrodeposition of germanium on molybdenum, the molybdenum partially delaminated from the SLG, hence germanium could not be used as bottom layer in this experimental set-up. Next, electrodeposited brass with a copper-to-zinc ratio of 1.7 prepared by the method in section 2.2 "Electrodeposition", was used as the bottom layer and did not suffer from this problem during germanium deposition. Mirror bright germanium coatings were deposited on the brass coating. Analysis of the composition of the brass/germanium stack
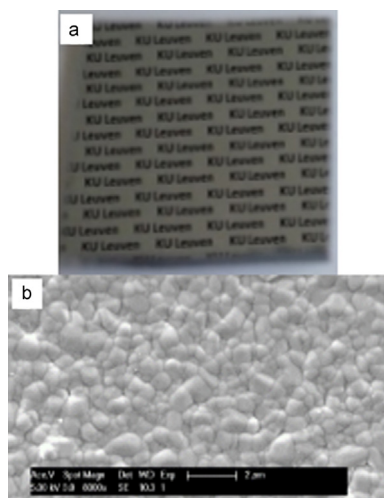

Fig. 10. Image (a) and top-view SEM image (b) of germanium deposited on a brass/tin stack on molybdenum-sputtered SLG ($20 \times 20\,mm^2$). Deposition of germanium from 5 vol% $GeCl_4$ in propylene glycol in a glove box (water and oxygen below 1 ppm), $j = -10\,A\,dm^{-2}$, mild stirring with magnetic stir bar, $T = 22\,°C$.

Table 3
Composition of brass/tin and brass/tin/germanium stacks on molybdenum-sputtered SLG (EDX).

	Before Ge deposition	After Ge deposition
Cu/at%	60	50 (57)
Zn/at%	23	20 (23)
Sn/at%	17	18 (20)
Ge/at%	–	12 (–)

The values between brackets are the copper, zinc and tin fractions without taking the germanium content into account.

showed that the copper/zinc ratio shifted from 1.7 to 4.2–4.6, hence the germanium plating bath affected the composition of the brass coating. Hot entry of the sample did not prevent the dissolution of brass, impeding the control of the composition of the final stack. In the third stacking order, germanium was deposited as the top layer on a brass/tin stack resulting in mirror bright, dense, closed coatings (Fig. 10). Analysis of the composition by EDX showed that no significant copper, zinc or tin losses occured during the electrodeposition of germanium (Table 3). Because of the low current efficiency (approximately 1.6%), the germanium coating thickness as a function of the deposition charge density deviated more from linearity ($R^2 = 0.88$) compared to the brass and tin electrolytes (Fig. 11). However, the composition of the brass/tin/germanium stack was still highly controlled by the deposition charge density.

3.4. Soft-annealing and selenization

Thermal pre-alloying, commonly referred to as "soft-annealing", has been shown to improve the homogeneity and compactness of kesterite films after selenization [47]. Furthermore, intermixing the precursors results in the formation of stable structures. Therefore, the brass/tin/germanium stacks were soft-annealed under a nitrogen atmosphere for 60 min at 350 °C. The appearance of the samples changed from lustrous gray before soft-annealing to matte gray after soft-annealing. XRD patterns of each step in the deposition process and of a complete stack after soft-annealing (with a thickness of approximately 950 nm) are shown in Fig. 12. The identification of the peak labels is shown in Table 4. The compositions are shown in Table 5. In all patterns, peaks related to the molybdenum substrate were recorded at 40.5°, 58.8° and 73.6°. The XRD pattern of the brass coating was characterized
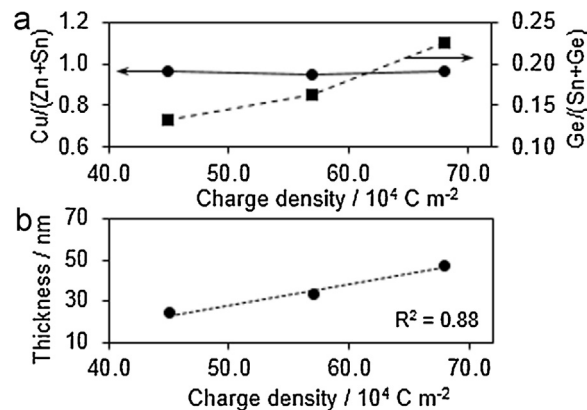

Fig. 11. $Cu/(Zn + Sn)$ ($\bullet$) and $Ge/(Sn + Ge)$ ($\blacksquare$) of the coating after electrodeposition of germanium (a) and thickness of the germanium coating (b) as a function of deposition charge density. Deposition of germanium from 5 vol% $GeCl_4$ in propylene glycol, $j = -10\,A\,dm^{-2}$, mild stirring, $T = 22\,°C$.
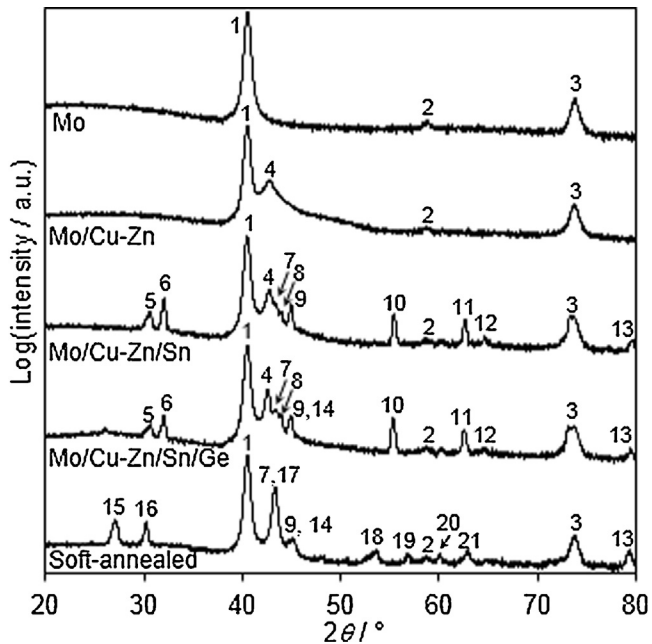
Fig. 12. XRD patterns of molybdenum-sputtered SLG, brass coating, brass/tin stack, brass/tin/germanium stack and brass/tin/germanium stack after soft-annealing (350 °C for 60 min). The peak labels are identified in Table 4. The composition of the coatings after each step in the production process is shown in Table 5.

by one additional peak at 42.6° (CuZn(110)). No peaks were attributed to a pure copper or zinc phase. Addition of a tin coating to the stack, resulted in the detection of several peaks related to pure tin. A peak attributed to a copper-tin binary phase ($Cu_{6.26}Sn_5(102)$) was detected at 43.2°. Copper-tin phases are known to form at room temperature due to the substantial diffusion rate of copper in tin [48]. The XRD pattern of the (as-deposited) brass/tin/germanium stack was characterized by an additional small peak at 45.0°, identified as Ge(220). Although this peak greatly overlapped with the Sn(211) peak, the presence of crystalline germanium is confirmed by Saitou et al., who deposited germanium from a similar electrolyte and detected Ge(220) as the sole germanium peak [27]. After soft-annealing under a nitrogen atmosphere for 60 min at 350 °C, a second germanium peak (Ge (111)) was detected at 27.1°. The soft-annealing also enabled the formation of a copper-germanium intermetallic compound, which resulted in the detection of the $Cu_5Ge_2(222)$ and $Cu_5Ge_2(400)$ planes at 53.6° and 62.8°, respectively. No elemental copper and zinc were detected. Copper was only detected as copper-germanium, copper-tin and copper-zinc alloy phases and zinc only as copper-zinc alloy phases. The presence of elemental tin could not be excluded with complete certainty because all tin

Table 4
Identification of the peaks recorded in the XRD patterns in Fig. 12.

Label	Crystal plane	Label	Crystal plane
1.	Mo(110)	12.	Sn(400)
2.	Mo(200)	13.	Sn(316)
3.	Mo(211)	14.	Ge(220)
4.	CuZn(110)	15.	Ge(111)
5.	Sn(200)	16.	CuZn(100)
6.	Sn(101)	17.	$Cu_5Zn_8(330)$
7.	$Cu_{6.26}Sn_5(102)$	18.	$Cu_5Ge_2(222)$
8.	Sn(220)	19.	$Cu_{5.31}Zn_{7.69}(521)$
9.	Sn(211)	20.	CuSn(103)
10.	Sn(301)	21.	$Cu_5Ge_2(400)$
11.	Sn(112)		

Table 5
Composition of as-deposited brass, brass/tin and brass/tin/germanium stacks and brass/tin/germanium stack after selenization. The CZTGSe samples were soft-annealed under a nitrogen atmosphere at 350 °C for 60 min and selenized with elemental selenium at 500 °C for 40 min.

Atomic ratio	Cu-Zn	Cu-Zn/Sn	Cu-Zn/Sn/Ge	CZTGSe
Cu/Zn	1.55 ± 0.02	1.49 ± 0.04		
Cu/(Zn + Sn)		0.96 ± 0.02	1.02 ± 0.02	
Cu/(Zn + Sn + Ge)			0.90 ± 0.02	0.90 ± 0.03
Zn/(Sn + Ge)			1.42 ± 0.03	1.34 ± 0.06
Ge/(Sn + Ge)			0.27 ± 0.02	0.30 ± 0.02

peaks greatly overlapped with copper-zinc and copper-tin peaks. No peaks could be attributed to binary zinc-tin phases because these elements do not form intermetallic compounds at these temperatures.

After soft-annealing, the coatings were selenized in the presence of elemental selenium at 500 °C for 40 min. After selenization, a dense, adherent film of closely packed micrometer-sized grains was obtained (Fig. 13). The composition of the coatings after each step of the process is shown in Table 5. As mentioned above, the composition of the coatings did not vary significantly after the deposition of successive coatings. Although other research groups reported the loss of germanium and/or tin during selenization [17,18], the composition of the coatings presented in our work, were not significantly influenced by soft-annealing and selenization of the brass/tin/germanium stacks. It is likely that the soft-annealing enabled the formation of stable (alloy) phases, which significantly hindered the formation of volatile compounds under the proposed selenization conditions.

The XRD pattern of the selenized film is shown in Fig. 14. Two peaks were related to molybdenum, i.e. at 40.5° (Mo(110)) and 73.6° (Mo(211)). The peaks at 31.7°, 55.9° and 66.2° were attributed to $MoSe_2$, i.e to $MoSe_2(101)$, $MoSe_2(110)$ and $MoSe_2(202)$, respectively. In kesterite solar cells, molybdenum is typically chosen as the back contact because of its good electrical and structural properties. However, thick molybdenum selenide layers have significantly less favorable electrical and structural properties [49], resulting in decreased solar cell performances. Because of the pronounced molybdenum selenide peaks in the XRD pattern, it is expected that the efficiency of the CZTGSe solar cell would be limited by its presence. Three other main peaks at 27.4°, 45.5° and 53.9° were related to the kesterite (112), (220) and (312) planes, respectively. It must be noted that the peak positions were shifted towards higher 2θ values compared to germanium-free CZTSe and lower values compared to tin-free CZGSe. By partially replacing the tin(IV) ions in CZTSe by smaller germanium(IV) ions, the lattice constants decrease, thus shifting the diffraction peaks to higher angles. Some additional minor peaks could be attributed to secondary phases: copper selenide, tin selenide and germanium selenide. Furthermore, the presence of zinc selenide could not be excluded because its diffraction peaks overlap almost entirely with the main kesterite peaks. The presence of these secondary phases, together with molybdenum selenide, are unfavorable for the production of high efficiency CZTGSe solar cells. From this structural study, it was concluded that germanium was successfully incorporated in the kesterite structure (because of the 2θ shift) and that further studies are required to minimize the presence of secondary phases after selenization.

3.5. Photoelectrochemical characterization

A CZTGSe film obtained by selenization at 520 °C for 40 min was photoelectrochemically characterized in order to obtain
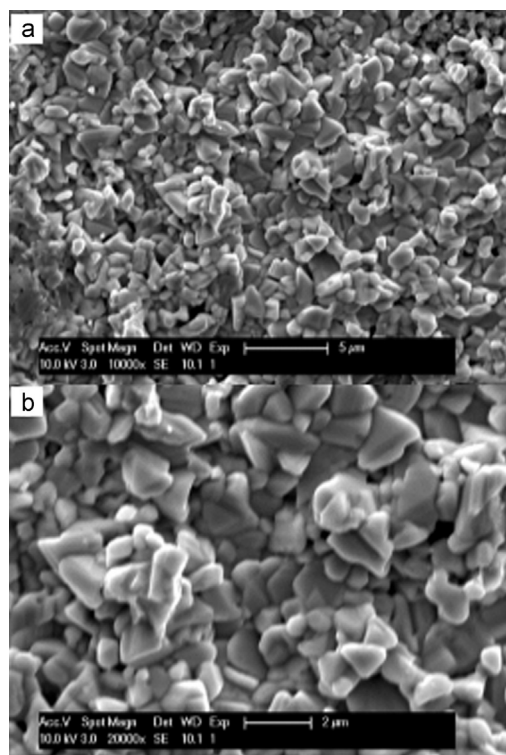
Fig. 13. Top-view SEM images of a coating after selenization with elemental selenium for 40 min at 500 °C; 10,000× (a) and 20,000× (b). Before selenization, the brass/tin/germanium stacks were soft-annealed for 60 min at 350 °C under a nitrogen atmosphere.

collected at the semiconductor/electrolyte interface, which implies that the CZTGSe behaved as a *p*-type semiconductor. The traces (B) and (C) correspond to the same film after 60 s etching with potassium cyanide and subsequent etching with hydrochloric acid.

The external quantum efficiencies recorded at 530 nm (i.e. difference between the equilibrium photocurrent and dark current divided by the photon flux) after sequential etching with potassium cyanide and hydrochloric acid is shown in Fig. 15b. The photocurrent was doubled by etching with potassium cyanide for 60 s, reaching an EQE(530 nm) of 5%. This is a very common phenomenon for chalcogenide semiconductor films, and is likely related to the removal of conductive Cu-Se phases from the surface acting as preferential paths for recombination of the charge carriers [31]. Subsequent etching steps with hydrochloric acid reduced the photocurrent, but modified the photocurrent transient substantially (i.e. it became more square) and generated a seemingly more ideal surface. The process seemed partially reversible, as a further potassium cyanide etching after hydrochloric acid treatment was able to restore the photocurrent to a slightly higher level. This suggests that hydrochloric acid possibly also had the effect of removing some detrimental phases from the surface of CZTGSe. Further iteration of etching steps resulted in a decrease of the photocurrent, suggesting that the optimal etching conditions consist of 30 s hydrochloric acid followed by 60 s potassium cyanide. Furthermore, the photocurrent onset of CZTGSe has been determined to be approximately −0.24 V vs. SHE, which is similar for that observed for CZTSe and CIGSe [52], suggesting a similar flat band potential. However, it needs to be mentioned that band edges of chalcogenide semiconductors in solution seem to be highly dependent on the surface oxidation state [53].

information on its optoelectronic properties, namely on its majority carrier type and ability to generate, collect and transport minority carriers under illumination to gain insights on its quantum efficiency. The effect of the removal of potentially detrimental secondary phases on the PEC properties of the film has also been investigated. For this purpose, consecutive surface etching treatments have been performed with potassium cyanide and hydrochloric acid solutions, which are known to remove secondary phases from the surface of the absorber material [50,51].

Fig. 15a shows the photocurrent transients of the as-deposited CZTGSe film (A) upon illumination with the 530 nm LED. The negative sign of the photocurrent indicates that electrons were
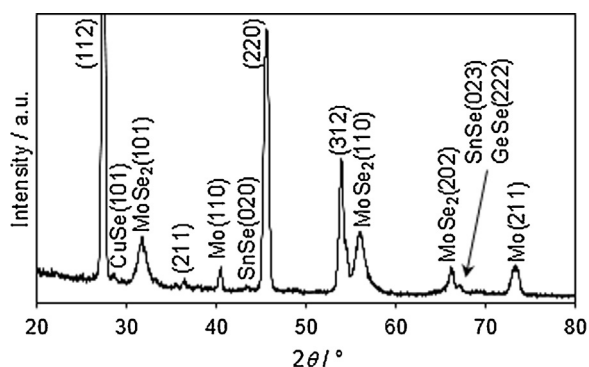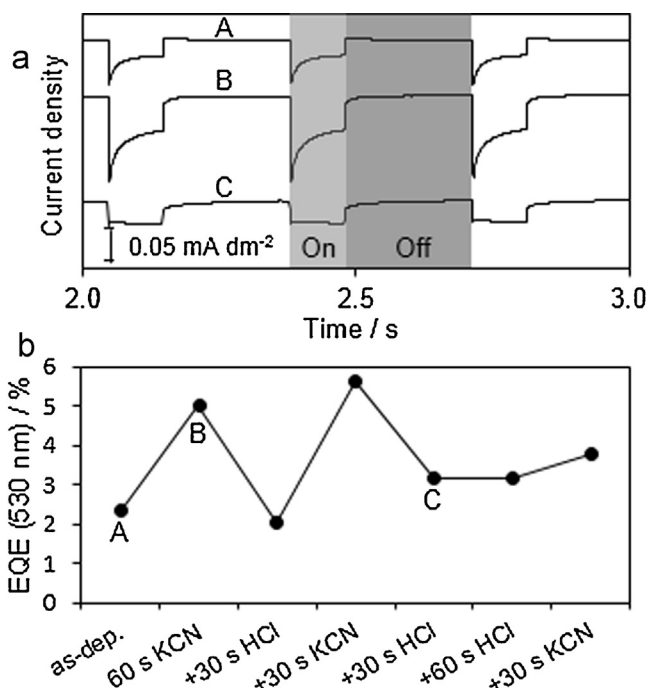

Fig. 14. XRD pattern of a CZTGSe coating on molybdenum-sputtered SLG after soft-annealing (350 °C for 60 min under a nitrogen atmosphere) and selenization with elemental selenium at 500 °C for 40 min. Peak identification is shown in the figure.

Fig. 15. Chronoamperometric tests after consecutive KCN and HCl etching steps as described in (b) in a 0.2 mol dm^{-3} Eu^{3+} solution at −0.59 V vs. SHE under pulsed illumination with a 530 nm LED (a) and external quantum efficiencies of a CZTGSe film after consecutive KCN and HCl etching steps (the lines are a guide to the eye) (b).
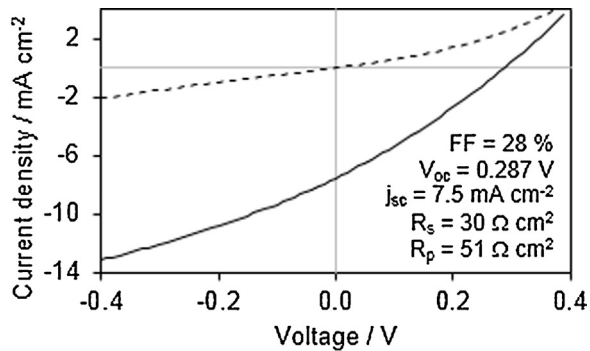
Fig. 16. Dark (dashed line) and illuminated (solid line) j-V characteristics of the best performing 0.25 cm^2 CZTGSe photovoltaic device (selenized for 40 min at 500 °C).

3.6. Photovoltaic device performance

After the photoelectrochemical characterization and optimization of the etching procedure, photovoltaic devices with a CZTGSe/CdS/i-ZnO/Al:ZnO configuration with a Ni/Al grid were prepared. The j-V characteristics of the photovoltaic device with the best performance are shown in Fig. 16. After correction for surface area and resistance of the electrical contact, it had a solar power conversion efficiency of 0.6% with a short circuit current density (j_{sc}) of 7.5 mA cm^{-2}, an open circuit voltage (V_{oc}) of 287 mV, a fill factor (FF) of 28%, a series resistance (R_s) of 30 Ω cm^2 and a parallel resistance (R_p) of 51 Ω cm^2. The series resistance is at least 1.5 orders of magnitude larger than its value in efficient devices, considerably reducing the short circuit current density and fill factor.

The band gap of the CZTGSe absorber film was calculated by two methods: determination of the inflection point (i.e. the maximum
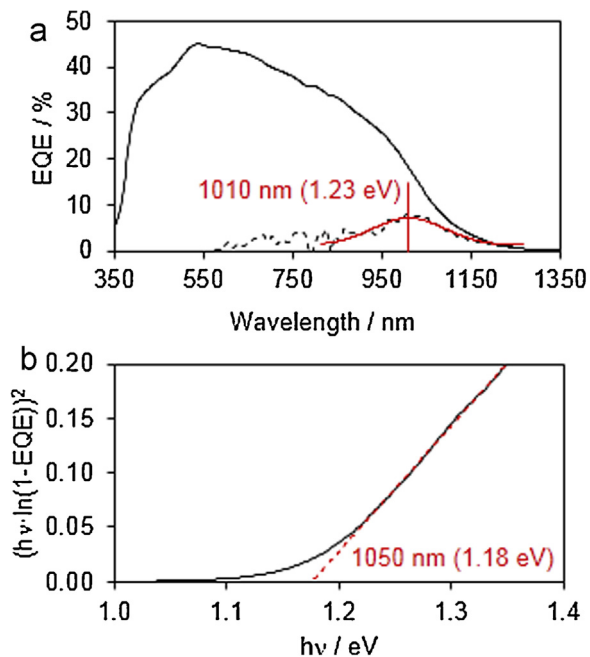
of $-dEQE/d\lambda$) (Fig. 17a) and by a linear fit of $(h\nu \cdot \ln(1-EQE))^2$ as a function of $h\nu$ (Fig. 17b). The inflection point was found to be 1010 nm, which corresponds to a band gap of 1.23 eV. In Fig. 17b, the linear fit crosses the $h\nu$-axis at 1.18 eV (1050 nm). Both methods give a band gap close to 1.2 eV, which is consistent with previously reported CZTGSe photovoltaic devices with Ge/(Sn + Ge) $\approx$ 0.40 with a band gap of 1.15 eV [18]. The band gap shift, together with the peak shift in the XRD patterns, leads to the conclusion that germanium was well included in the crystal structure of the absorber material and that the proposed electrodeposition-annealing route enabled the production of CZTGSe photovoltaic devices. A structural study of the (soft-) annealing conditions and etching process are expected to further improve the performance of the devices.

4. Conclusions

In this work, CZTGSe absorber material for photovoltaic devices was prepared by an electrodeposition-annealing approach. The electrochemical approach enabled the fabrication of uniform, dense, closed brass/tin/germanium stacks without the use of hazardous compounds, such as hydrazine. The composition of the brass coating was independent of the charge density. The thickness and the composition of the complete stack could easily be tuned by control of the deposition charge of each coating and with special attention for exchange reactions. The selenized coatings consisted of closely packed micrometer-sized grains together with smaller grains. XRD and photocurrent spectroscopy showed that germanium was successfully incorporated in the kesterite structure. The CZTGSe photovoltaic device with the best performance showed a solar power conversion efficiency of 0.6 % with a band gap near 1.2 eV, which is consistent with Ge/(Sn + Ge) $\approx$ 0.40 [18]. It is therefore concluded that the proposed electrodeposition-annealing approach leads to the successful incorporation of germanium in the crystal structure of the absorber material, enabling the production of CZTGSe absorber material with the desired copper-poor and zinc-rich composition for photovoltaic devices. In further studies of the selenization procedure, the presence of the secondary phases copper selenide, tin selenide, zinc selenide and germanium selenide, together with a molybdenum selenide layer between the kesterite and the molybdenum back contact, should be minimized in order to increase the efficiency.

Fig. 17. EQE (solid line), $-dEQE/d\lambda$ (dashed line) and fit of $-dEQE/d\lambda$ (a) and $(h\nu \cdot \ln(1-EQE))^2$ as a function of $h\nu$ (solid line) with linear fit (dashed line) (b). Measurements were performed on the 0.25 cm^2 CZTGSe photovoltaic device with the best performance (selenized for 40 min at 500 °C).

References

[1] A. Colthorpe, Solar Frontier's record efficiency 22.3% CIS cell faces 'global market challenge', Internet http://www.pv-tech.org/news/solar-frontiers-record-efficiency-22.3-cis-cell-faces-global-market-challen, December 8, 2015.
[2] M.A. Green, K. Emery, Y. Hishikawa, W. Warta, E.D. Dunlop, Solar cell efficiency tables (version 46), Prog. Photovoltaics 23 (2015) 805.
[3] W.D. Cyrs, H.J. Avens, Z.A. Capshaw, R.A. Kingsbury, J. Sahmel, B.E. Tvermoes, Landfill waste and recycling: use of a screening-level risk assessment tool for end-of-life cadmium telluride (CdTe) thin-film photovoltaic (PV) panels, Energy Policy 68 (2014) 524.

[4] G. Phipps, C. Mikolajczak, T. Guckes, Indium and gallium: long-term supply, Renew. Energy Focus 9 (2008) 56.

[5] M. Jiang, X. Yan, Cu_2ZnSnS_4 thin film solar cells: present status and future prospects, in: A. Morales-Acevedo (Ed.), Solar cells—Research and application perspectives, InTech, Rijeka (Croatia), 2013, pp. 107.

[6] M.P. Suryawanshi, G.L. Agawane, S.M. Bhosale, S.W. Shin, P.S. Patil, J.H. Kim, A.V. Moholkar, CZTS based thin film solar cells: a status review, Mater. Technol. 8 (2013) 98.

[7] C. Persson, Electronic and optical properties of Cu_2ZnSnS_4 and $Cu_2ZnSnSe_4$, J. Appl. Phys. 107 (2010) 053710.

[8] W. Wang, M.T. Winkler, O. Gunawan, T. Gokmen, T.K. Todorov, Y. Zhu, D.B. Mitzi, Device characteristics of CZTSSe thin-film solar cells with 12.6% efficiency, Adv. Energ. Mat. 4 (2014) 1301465.

[9] M. Frenzel, M.P. Ketris, J. Gutzmer, On the geological availability of germanium, Miner Deposita 49 (2014) 471.

[10] D.E. Guberman, Mineral commodity summaries 2016: germanium, United States Geological Survey, 2016, pp. 70.

[11] C.S. Anderson, Mineral Commodity Summaries 2015: tin, United States Geological Survey (2015) 174.

[12] B. Robertz, J. Verhelle, M. Schurmans, The primary and secondary production of germanium: a life-cycle assessment of different process alternatives, Jom-Us 67 (2015) 412.

[13] F. Luckert, D.I. Hamilton, M.V. Yakushev, N.S. Beattie, G. Zoppi, M. Moynihan, I. Forbes, A.V. Karotki, A.V. Mudryi, M. Grossberg, J. Krustok, R.W. Martin, Optical properties of high quality $Cu_2ZnSnSe_4$ thin films, Appl. Phys. Lett. 99 (2011) 062104.

[14] H. Matsushita, T. Ochiai, A. Katsui, Preparation and characterization of $Cu_2ZnGeSe_4$ thin films by selenization method using the Cu-Zn-Ge evaporated layer precursors, J. Cryst. Growth 275 (2005) E995.

[15] Y.B. Zhang, X.D. Sun, P.H. Zhang, X. Yuan, F.Q. Huang, W.Q. Zhang, Structural properties and quasiparticle band structures of Cu-based quaternary semiconductors for photovoltaic applications, J. Appl. Phys. 111 (2012) 063709.

[16] K. Biswas, S. Lany, A. Zunger, The electronic consequences of multivalent elements in inorganic solar absorbers: multivalency of Sn in Cu_2ZnSnS_4, Appl. Phys. Lett. 96 (2010) 201902.

[17] C.J. Hages, S. Levcenco, C.K. Miskin, J.H. Alsmeier, D. Abou-Ras, R.G. Wilks, M. Bär, T. Unold, R. Agrawal, Improved performance of Ge-alloyed CZTGeSSe thin-film solar cells through control of elemental losses, Prog. Photovolt. Res. Appl. 23 (2013) 376.

[18] Q. Guo, G.M. Ford, W.-C. Yang, C.J. Hages, H.W. Hillhouse, R. Agrawal, Enhancing the performance of CZTSSe solar cells with Ge alloying, Sol. Energ. Mat. Sol. Cells 105 (2012) 132.

[19] G.M. Ford, Q.J. Guo, R. Agrawal, H.W. Hillhouse, Earth abundant element Cu_2Zn $(Sn_{1-x}Ge_x)S_4$ nanocrystals for tunable band gap solar cells: 6.8% efficient device fabrication, Chem. Mater. 23 (2011) 2626.

[20] M. Buffière, H. ElAnzeery, S. Oueslati, K. Ben Messaoud, G. Brammertz, M. Meuris, J. Poortmans, Physical characterization of $Cu_2ZnGeSe_4$ thin films from annealing of Cu-Zn-Ge precursor layers, Thin Solid Films 582 (2015) 171.

[21] S. Levcenko, R. Caballero, E. Dermenji, E.V. Telesh, I.A. Victorov, J.M. Merino, E. Arushanov, M. Leon, I.V. Bodnar, Preparation and optical characterization of $Cu_2ZnGeSe_4$ thin films, Opt. Mater. 40 (2015) 76.

[22] S. Bag, O. Gunawan, T. Gokmen, Y. Zhu, D.B. Mitzi, Hydrazine-processed Ge-substituted CZTSe solar cells, Chem. Mater. 24 (2012) 4588.

[23] D. Colombara, A. Crossay, L. Vauche, S. Jaime, M. Arasimowicz, P.P. Grand, P.J. Dale, Electrodeposition of kesterite thin films for photovoltaic applications: quo vadis? Phys. Status Solidi A 212 (2015) 88.

[24] J.J. Scragg, D.M. Berg, P.J. Dale, A 3.2% efficient kesterite device from electrodeposited stacked elemental layers, J. Electroanal. Chem. 646 (2010) 52.

[25] Modern Electroplating, in: M. Schlesinger, M. Paunovic (Eds.), 5 ed., John Wiley & Sons, Hoboken (USA), 2010.

[26] C.G. Fink, V.M. Dokras, Electrodeposition and electrowinning of germanium, J. Electrochem. Soc. 95 (1949) 80.

[27] M. Saitou, K. Sakae, W. Oshikawa, Evaluation of crystalline germanium thin films electrodeposited on copper substrates from propylene glycol electrolyte, Surf. Coat. Technol. 162 (2003) 101.

[28] M.X. Wu, N.R. Brooks, S. Schaltin, K. Binnemans, J. Fransaer, Electrodeposition of germanium from the ionic liquid 1-butyl-1-methylpyrrolidinium dicyanamide, Phys. Chem. Chem. Phys. 15 (2013) 4955.

[29] M.X. Wu, G. Vanhoutte, N.R. Brooks, K. Binnemans, J. Fransaer, Electrodeposition of germanium at elevated temperatures and pressures from ionic liquids, Phys. Chem. Chem. Phys. 17 (2015) 12080.

[30] Y. Aida, V. Depredurand, J.K. Larsen, H. Arai, D. Tanaka, M. Kurihara, S. Siebenritt, Cu-rich $CuInSe_2$ solar cells with a Cu-poor surface, Prog. Photovolt.: Res. Appl. 23 (2015) 754.

[31] D. Colombara, A. Crossay, D. Regesch, C. Broussillou, T.G. de Monsabert, P.P. Grand, P.J. Dale, Prediction of photovoltaic p-n device short circuit current by photoelectrochemical analysis of p-type CIGSe films, Electrochem. Commun. 48 (2014) 99.

[32] K. Clauwaert, K. Binnemans, E. Matthijs, J. Fransaer, Electrochemical studies of the electrodeposition of copper-zinc-tin alloys from pyrophosphate electrolytes followed by selenization for CZTSe photovoltaic cells, Electrochim. Acta 188 (2016) 344.

[33] E. Deltombe, N. De Zoubov, M. Pourbaix, Molybdenum, in: M. Pourbaix (Ed.), Atlas of electrochemical equilibria in aqueous solutions, National Association of Corrosion Engineers, Houston (USA), 1974, pp. 272.

[34] P.P. Prosini, M.L. Addonizio, A. Antonaia, Effect of substrate surface treatment on the nucleation and crystal growth of electrodeposited copper and copper-indium alloys, Thin Solid Films 298 (1997) 191.

[35] O.E. Schupp III, P.E. Sturrock, J.I. Watters, A study of the stability and basicity of the copper(II) pyrophosphate complexes using the dropping amalgam electrode, Inorg. Chem. 2 (1963) 106.

[36] L.G. Sillen, A.E. Martell, Stability constants of metal-ion complexes, Chemical Society, London (UK), 1964.

[37] H. Konno, M. Nagayama, Mechanism of electrodeposition of copper from cupric pyrophosphate solutions, Electrochim. Acta 22 (1977) 353.

[38] H. Konno, M. Nagayama, The role of pyrophosphate in copper deposition from cupric pyrophosphate solutions, Electrochim. Acta 23 (1978) 1001.

[39] K. Johannsen, D. Page, S. Roy, A systematic investigation of current efficiency during brass deposition from a pyrophosphate electrolyte using RDE RCE, and QCM, Electrochim. Acta 45 (2000) 3691.

[40] D. Sylla, C. Savall, M. Gadouleau, C. Rebere, J. Creus, P. Refait, Electrodeposition of Zn-Mn alloys on steel using an alkaline pyrophosphate-based electrolytic bath, Surf. Coat. Tech. 200 (2005) 2137.

[41] J.J. Scragg, P.J. Dale, L.M. Peter, Synthesis and characterization of Cu_2ZnSnS_4 absorber layers by an electrodeposition-annealing route, Thin Solid Films 517 (2009) 2481.

[42] M. Kurihara, D. Berg, J. Fischer, S. Siebenritt, P.J. Dale, Kesterite absorber layer uniformity from electrodeposited precursors, Phys. Status Solidi C 6 (2009) 1241.

[43] J.R. Duffield, D.R. Williams, I. Kron, Speciation studies of the solubility and aqueous-solution chemistry of tin(II) pyrophosphate and tin(IV) pyrophosphate complexes, Polyhedron 10 (1991) 377.

[44] E. Deltombe, N. De Zoubov, C. Vanleugenhaghe, M. Pourbaix, Tin, in: M. Pourbaix (Ed.), Atlas of electrochemical equilibria in aqueous solutions, National Association of Corrosion Engineers, Houston (USA), 1974, pp. 475.

[45] X.C. He, H.L. Shen, J.H. Pi, C.X. Zhang, Y. Hao, Synthesis of Cu_2ZnSnS_4 films from sequentially electrodeposited Cu-Sn-Zn precursors and their structural and optical properties, J. Mater. Sci.: Mater. Electron. 24 (2013) 4578.

[46] N. De Zoubov, M. Pourbaix, Zinc, in: M. Pourbaix (Ed.), Atlas of electrochemical equilibria in aqueous solutions, National Association of Corrosion Engineers, Houston (USA), 1974, pp. 406.

[47] Y. Lin, S. Ikeda, W. Septina, Y. Kawasaki, T. Harada, M. Matsumura, Mechanistic aspects of preheating effects of electrodeposited metallic precursors on structural and photovoltaic properties of Cu_2ZnSnS_4 thin films, Sol. Energ. Mat. Sol. Cells 120 (2014) 218.

[48] H.C. Bhedwar, V. Balasubr, S.D. Kulkarni, K.K. Ray, Kirkendall effect studies in copper-tin diffusion couples, Scripta Metall. Mater. 6 (1972) 919.

[49] A. Jager-Waldau, M.C. Lux-Steiner, E. Bucher, L. Scandella, A. Schumacher, R. Prins, MoS_2 thin-films prepared by sulfurization, Appl. Surf. Sci. 65–6 (1993) 465.

[50] M. Weber, R. Scheer, H.J. Lewerenz, H. Jungblut, U. Sturkel, Microroughness and composition of cyanide-treated $CuInS_2$, J. Electrochem. Soc. 149 (2002) G77.

[51] A. Fairbrother, E. Garcia-Hemme, V. Izquierdo-Roca, X. Fontane, F.A. Pulgarin-Agudelo, O. Vigil-Galan, A. Perez-Rodriguez, E. Saucedo, Development of a selective chemical etch to improve the conversion efficiency of Zn-rich Cu_2ZnSnS_4 solar cells, J. Am. Chem. Soc. 134 (2012) 8018.

[52] J.J. Scragg, P.J. Dale, L.M. Peter, G. Zoppi, I. Forbes, New routes to sustainable photovoltaics: evaluation of Cu_2ZnSnS_4 as an alternative absorber material, Phys. Status Solidi B 245 (2008) 1772.

[53] W. Siripala, J. Vedel, D. Lincot, D. Cahen, Band edge shifts of p-type copper indium diselenide electrodes in aqueous-electrolytes, Appl. Phys. Lett. 62 (1993) 519.